scientific reports

OPEN

Finite element analysis of the seismic performance of wind and rain bridge

Wenke Yuan[1], Ting Ding[1✉], Xiaokang Hu[1,2] & Jiaxin Liu[1,2]

The traditional architecture of the Dong and other ethnic minorities show cases unique architectural skills. Its conservation is significant for maintaining the diversity of national culture and transmitting traditional craftsmanship. This study used ABAQUS software to analyse the mechanical properties of two typical wind and rain bridge structures. The results show that the arch bridge structure of Model 2 is significantly better than the simply supported beam bridge structure of Model 1 in terms of load-bearing capacity. Specifically, the mid-span deflection of Model 2 is only approximately 7% of that of Model 1. In addition, the El-Centro seismic wave was selected as the excitation data for this study, and the time-history analysis was performed according to the 7-degree seismic fortification standard. The results demonstrate that the arch bridge structure of Model 2 also performs well in terms of seismic performance, with lower acceleration responses at both mid-span analysis points compared to that of Model 1. These findings provide a scientific basis for the structural optimisation of wind and rain bridges and offer valuable insights into the modern conservation and continuation of traditional architectural heritage.

As of 2024, UNESCO reports 1,223 World Heritage Sites across 168 countries, including 59 in China: 40 cultural, 15 natural, and 4 mixed cultural-natural sites. Cultural heritage, a cornerstone of human civilization, fosters cultural identity, social cohesion, and tourism while supporting creative economies. As an important carrier of human civilization, cultural heritage plays is essential in fostering cultural identity, shaping cultural characters, bridging cultural divides, and facilitating the development of tourism and cultural and creative economy[1]. Its preservation sustains national heritage, drives educational and economic progress, fosters innovation, and promotes ecological balance, bridging past wisdom with future development[2]. In recent years, the rapid development of digital technology has introduced new opportunities and challenges for protecting traditional cultural heritage. For example, the application of remote sensing technology enables high-precision documentation of heritage structures like ancient bridges, supporting digital archiving and structural modelling for scientific research[3,4]. Meanwhile, finite element analysis software provides comprehensive and in-depth scientific support for the structural performance study of cultural heritage through efficient calculation and simulation[5]. The application of these technologies enhances the accuracy and scientific rigour of cultural heritage protection and opens up new paths for the sustainable utilization and dissemination of cultural heritage.

Wind and Rain Bridge is a typical representative of traditional wooden bridges in China, which are mainly located in the minority areas in Southwest China, particularly among the Dong ethnic minority. Wind and rain bridges adopt mortise and tenon structures without nails, and the bridge body consists of piers, corridors and pavilions, with benches and railings on both sides of the corridors. In contrast, the pavilions are mostly multi-story gable-type buildings, which also serve the function of sheltering from the wind and rain[6–8]. Most of the wind and rain bridges are designed in the form of mortise and tenon structures to support heavy loads[9,10]. Wind and rain bridges are exemplars of architectural art, carrying the history, religion and social life of the Dong people and offering significant historical and cultural research value.

These wooden bridges are vulnerable to natural erosion, human damage, and seismic risks, exacerbated by urbanization, threatening their survival. Earthquakes pose a severe threat, loosening or fracturing joints under cyclic loads, causing instability, while mismatched vibration responses between piers and decks risk localized or total collapse[11,12]. In addition, wind and rain bridges are mostly built in mountainous areas or near rivers, and earthquakes may also trigger secondary disasters such as landslides, mudslides, and floods, further aggravating

[1]College of Civil Engineering, Guizhou University, Guiyang 550025, China. [2]Xiaokang Hu and Jiaxin Liu These authors contributed equally to this work. ✉email: tding1@gzu.edu.cn

their damage. Compared to studies on reinforced concrete and steel structures, there is an extreme lack of research in the literature on the behaviour and performance of timber bridges (especially traditional ones). This knowledge gap is further expanding as the scope of structural design is gradually extended to extreme loads caused by multiple hazards[13,14]. Studying their load-sharing structures and seismic performance is crucial for preservation, informing seismic design, modernizing traditional techniques, and promoting resilient, sustainable heritage conservation. Regarding material properties, wood anisotropy parameters were determined experimentally and theoretically. Experimentally, mechanical tests (tensile/compression/shear) were carried out along the longitudinal, radial, and tangential directions to determine the modulus of elasticity, Poisson's ratio, and other parameters, supplemented by ultrasonic[15] or vibrational modal analyses[16,17] to obtain the dynamic properties. Theoretically, an orthogonal anisotropic model is established based on the microstructure, scale simulation is used to correlate the macro-mechanics with the microscopic features, and humidity and density correction coefficients are introduced to optimise the applicability of the parameters. However, existing research predominantly focuses on qualitative descriptions of architectural features or historical significance, while quantitative mechanical analyses of traditional timber bridges remain scarce, especially regarding the comparative seismic performance between distinct structural typologies, such as simply supported and arch configurations. This gap limits the scientific basis for optimizing the structural forms in heritage conservation. To address this, our study employs high-fidelity finite element modeling to quantitatively assess and compare the static bearing capacity and dynamic seismic responses of two representative wind and rain bridge archetypes. By integrating modern computational mechanics with traditional structural characteristics, we provide an analysis of the results of the stiffness distribution and stress concentrations specific to these culturally significant structures.

In recent years, finite element analysis (FEA) software has become indispensable in modern engineering design. ABAQUS, a versatile FEA tool, excels in aerospace, automotive, and civil engineering due to its robust nonlinear analysis capabilities and extensive material library[18–20]. It accurately simulates complex structural behaviours under diverse loading conditions, addressing challenges like large deformations, contact nonlinearities, and material nonlinearity. Additionally, it supports multiphysics coupling, heat transfer, and fluid dynamics, enabling comprehensive engineering optimization[21–23]. By predicting stress distribution, deformation, and failure modes early in design stages, ABAQUS reduces experimental costs, accelerates R&D cycles, and enhances structural safety. Its high-fidelity simulations also drive innovation in materials and structural technologies. With advancing computational power and software features, FEA applications in engineering are poised for further expansion. Finite element analysis (FEA) is a numerical computing technique that simulates complex systems by discretizing continuous structures into finite numbers of cells. The core steps include modeling and meshing, defining material parameters and boundary conditions, and establishing and solving numerical solutions. This method has made important progress in basic theory and applied research (e.g., material property simulation[11,24,25] and three-dimensional simulation[26,27]).

Regarding seismic analysis methods, time-history analysis and the inelastic response spectrum method are the two most commonly used approaches. Time-history analysis[28,29] is used as a base method to ensure accurate capture of the dynamic response. The inelastic spectral method achieves fast performance prediction through simplified models and regression analysis[30]. The advantage of time-history analysis over inelastic spectral methods is its ability to handle complex nonlinear and dynamic effects. However, its use must be weighed against the computational cost and the accuracy of the model details. It is particularly suitable for prefabricated structures where P-Delta effects and displacements must be tightly controlled, providing a theoretical basis and practical tool for their seismic design.

This study analyzes two wind and rain bridge models, a simply supported beam bridge (Model 1) and an arch bridge (Model 2), using ABAQUS to evaluate load-bearing capacity and seismic performance. Firstly, based on actual bridge geometries and material properties, high-fidelity finite element models underwent static load and modal analyses to assess stress and vibration characteristics. Secondly, the intrinsic frequencies and vibration shapes of the two structures were determined by modal analysis, and the dynamic responses under a 7-degree seismic fortification standard were simulated by inputting El-Centro seismic waves using the time-history analysis method. This provides a scientific basis for the optimizing design and seismic reinforcement of the traditional wind and rain bridge. Using ABAQUS, three-dimensional finite element models were developed, advancing the analysis of nonlinear behavior in wooden structures beyond traditional two-dimensional approaches. In the finite element modelling, local coordinate systems were rigorously defined at the joints and curved sections to align the orthotropic material axes with the grain direction, ensuring an accurate representation of the anisotropic behavior in complex geometries[31,32]. In addition, the study innovatively combines modern finite element technology with the needs of cultural heritage protection, which not only constructs a nonlinear contact algorithm system applicable to wooden bridges but also provides a digital evaluation paradigm for the seismic reinforcement of traditional buildings, and realizes the interdisciplinary fusion of engineering mechanical analysis and intangible cultural heritage protection. Finally, this study provides a brief overview of the design of vibration-damping techniques, including dampers[33], rubber isolators[34], and Seesaw systems[35], is provided, drawing on existing literature[36–38], to enhance structural resilience.

The model of wind and rain bridge
Characteristics of wind and rain bridge structural and project overview
Wind and rain bridge is a traditional building unique to the ethnic minority areas in southern China, which is mainly made of wood structure, using mortise and tenon joints without the need for nails. The bridge is topped with a pavilion or roof, which serves both as a shelter from the wind and rain and as a resting place, with railings and benches on both sides. The bridge piers are mostly stone structures, which are stable and durable. Adorned with intricate ethnic carvings, the brigdes reflect rich cultural heritage. This paper refers to Chengyang Yongji

Bridge and Xijiang Thousand Households Miaozhai Longtan Bridge, comparing the load-bearing capacity and seismic performance of the two types of wind and rain bridges.

Chengyang Yongji Bridge, located in Sanjiang Dong Autonomous County of Guangxi Zhuang Autonomous Region, is one of the masterpieces of Dong wind and rain bridges. The bridge is 64.4 m long, 3.4 m wide and 10.6 m high, consisting of five bridge pavilions and nineteen bridge corridors. Xijiang Longtan Bridge is located in Leishan County, Guizhou Province, and is a typical representative of the Miao wind and rain bridge. The bridge spans over the Longtan River, with a total length of about 50 m and an arch-shaped body. Both bridges are made of wood and stone, with the piers made of masonry and the corridors and pavilions all made of wood, mortise and tenon joints, with exquisite craftsmanship. The roofs of the bridges are covered with green tiles, and there are railings and benches on both sides of the bridge corridors for pedestrians to rest. The real scene pictures of the two bridges are shown in Fig. 1.

Geometric modelling and meshing method

Model 1 is modelled after the Chengyang Yongji Bridge. The model is a three-span supported bridge structure. The bridge comprises three independent spans, with timber bearings between the bridge deck and piers, which are connected to the bridge by mortise and tenon joints. Model 2 is modeled after the Xijiang Longtan Bridge. The model is a single-span arch bridge structure. Three small arches are built symmetrically on the two arch shoulders of the bridge. Both models have the same dimensions, with a span of 76 m and a deck width of 4.3 m. The Axonometric drawing and Plan view of the two models are shown in Fig. 2 and Fig. 3.

Specifically, Model 1 adopts a three-span supported system, with three independent span segments forming a segmental static structure through the timber bearings. Each span section forms its bending moment system under static force, and the positive bending moment reaches its peak value in the middle of the span. At the same time, there is no bending moment transfer at the bearing. The load is transferred to the abutment step by step through the deck slab and timber bearing, allowing the independent vertical displacement of each span, which is more adaptable to the settlement of the foundation.

In contrast, Model 2 is a single-span arch bridge, with the main arch ring constituting a continuous thrust structure, which converts the vertical load into axial pressure, and the bending moment distribution presents parabolic characteristics. The three small hollow arches on the arch shoulder form a multi-hole continuous

a)

b)

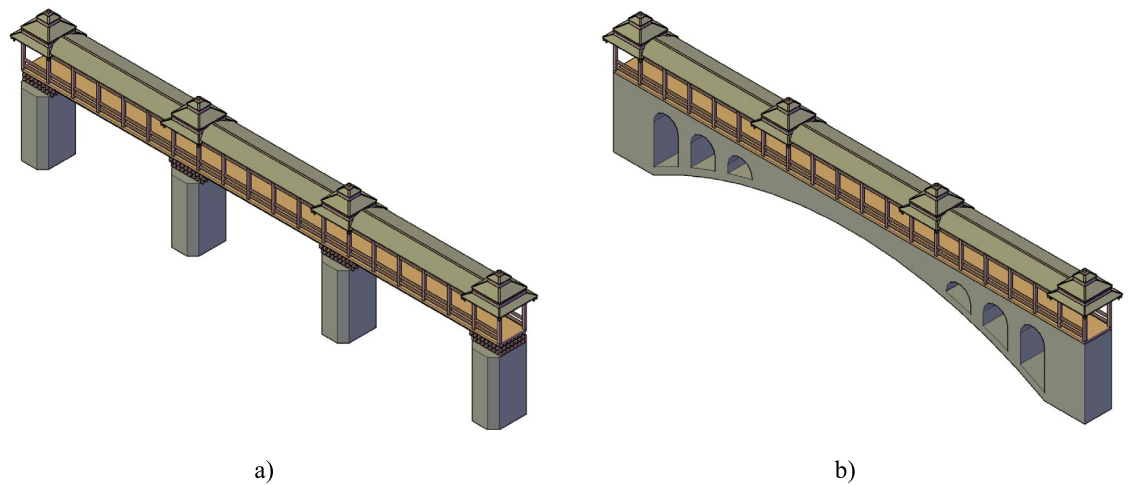**Fig. 1**. Actual view of the bridge. **a**) Chengyang Yongji Bridge (Source: https://www.sohu.com/a/311908103_6 93606) **b**) Xijiang Longtan Bridge (Source: https://touch.travel.qunar.com/comment/5383199?from=client).

Fig. 2. Axonometric drawing of a model bridge based on AutoCAD 2020 (URL: https://www.autodesk.com/products/autocad/overview).
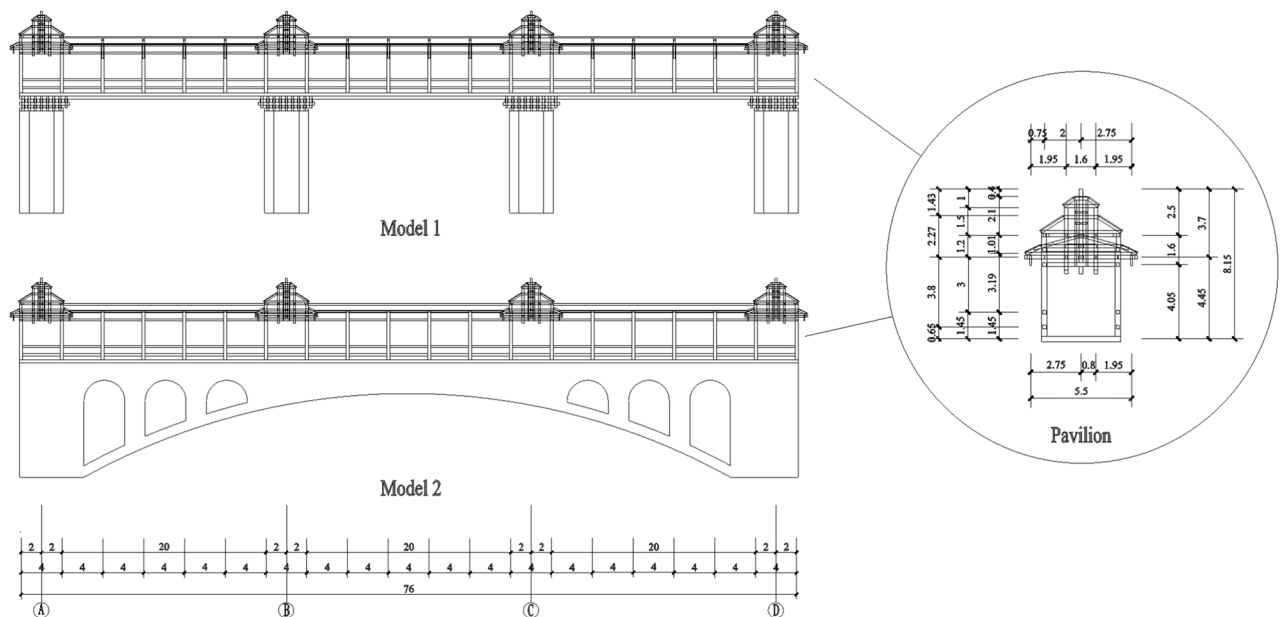
Fig. 3. Plan view of the model bridge (m) based on AutoCAD 2020 (URL: https://www.autodesk.com/products/autocad/overview).

arch effect, which significantly improves the overall stiffness. Loads are transferred directly from the arch superstructure to the arch base foundation, ensuring greater structural integrity.

In addition, the two models'superstructures, i.e., the corridor and pavilion parts, of the two models are identical. The four square pavilions are arranged equidistant from each other and are connected by a corridor in the centre. Figure 4 shows the expanded view of the model superstructure.

The columns in the superstructure are modelled with a square cross-section of 0.3m × 0.3m, with a total arrangement of 40 columns. Therefore, the contact area of the superstructure with the bridge deck is

$$S_p = 0.3 \times 0.3 \times 40 = 3.6m^2 \tag{1}$$

In finite element analysis, a coarse mesh is usually used to simulate the overall behaviour and a fine mesh is used for more detailed local analysis. For both models, a coarse mesh with an approximate global seed size of 500 mm is applied to the bridge body, including piers and superstructure components. The fine mesh is mainly used to divide the bridge deck, taking the approximate global size of 100 mm for seeding. The meshing of the two models is illustrated in Fig. 5.
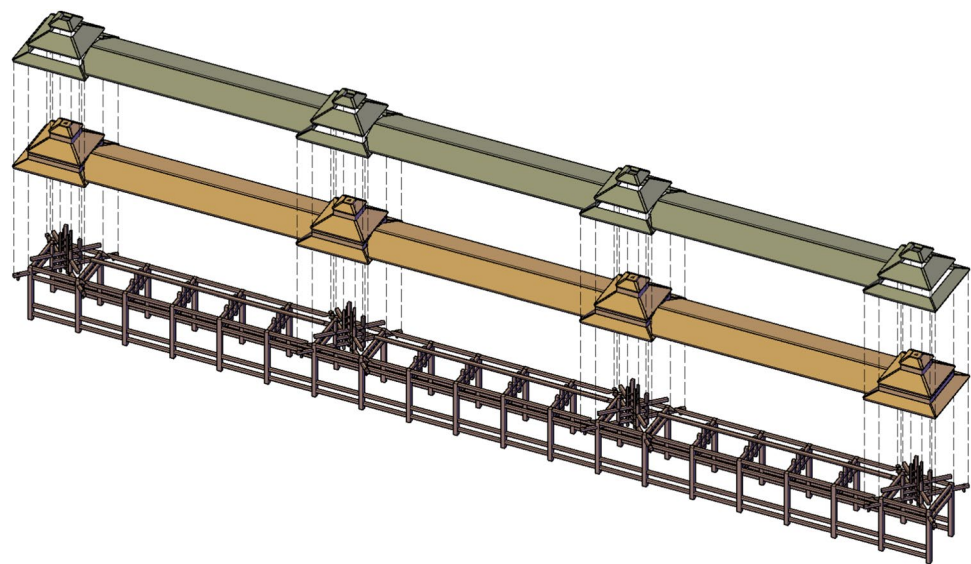
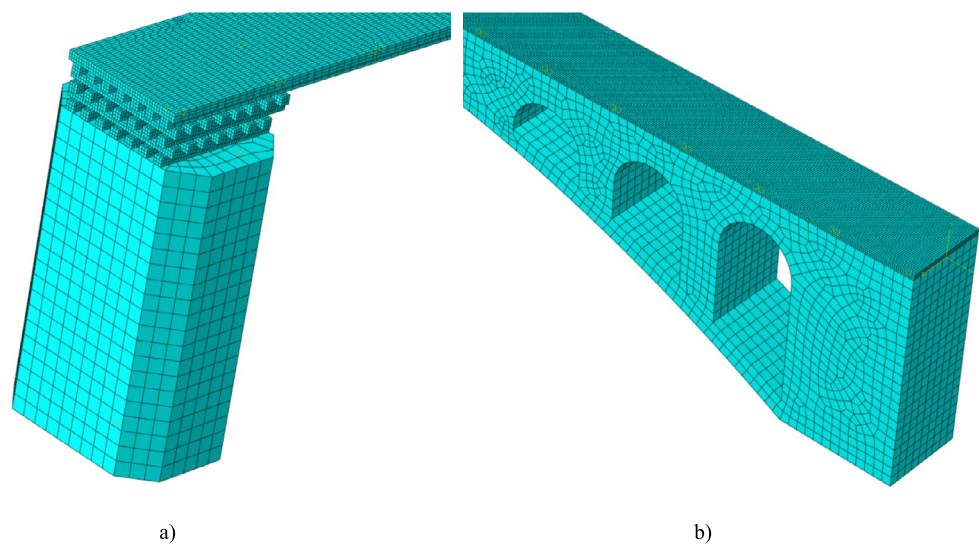**Fig. 4**. Exploded view of the bridge superstructure (corridors and pavilions) based on AutoCAD 2020 (URL: https://www.autodesk.com/products/autocad/overview).

a)   b)

Fig. 5. Meshing method based on ABAQUS 2024 (URL: https://www.3ds.com/products/simulia/abaqus).

E_1	E_2	E_3	Nu_{12}	Nu_{13}	Nu_{23}	G_{12}	G_{13}	G_{23}
11,000	900	900	0.43	0.43	0.63	910	910	79
f	R_{11}	R_{22}	R_{33}	R_{12}	R_{13}	R_{23}		
35	1	0.123	0.123	0.197	0.197	0.197		

Table 1. Properties of wood.

Material parameters and load calculations

The wind and rain bridge models incorporate distinct materials for the superstructure and substructure. The pavilon roofs are covered with green tiles, with a density of ρ_t=1800 kg/m³. The wooden components, including corridors, pavilions, and the bridge deck, have a density of ρ_w=500 kg/m³. The wood is anisotropic material, and the parameters of the chosen wood are shown in Table 1.
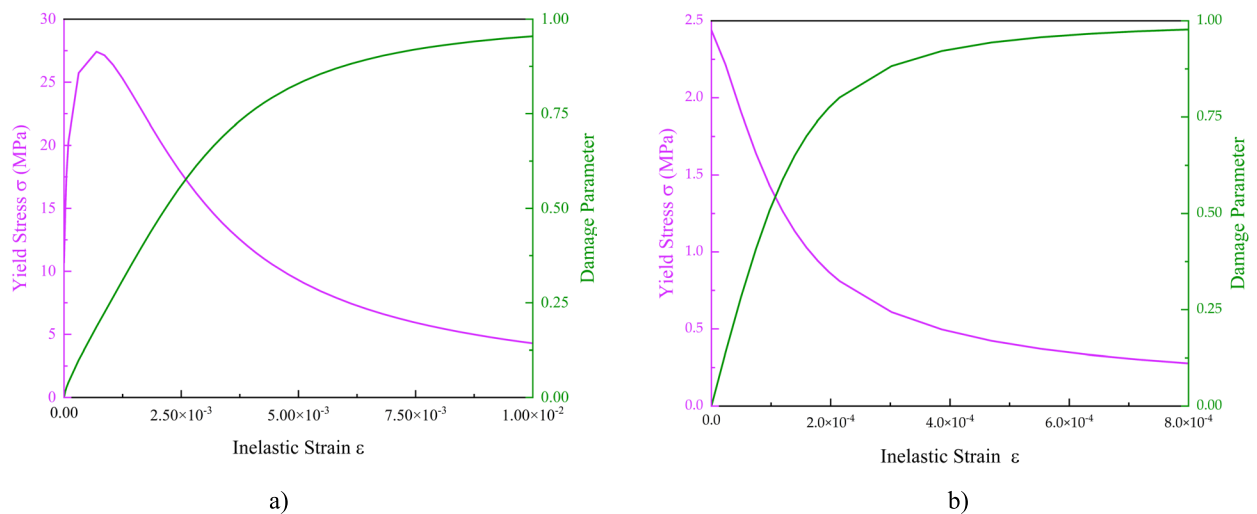
a)

b)

Fig. 6. Intrinsic model of the selected concrete based on Origin 2021 (URL: https://www.originlab.com/).

Superstructure component	Materials	Volume (m³)	Density (kg/m³)
Corridor and pavilion frames	wood	$V_1 = 57.2069$	500
Corridor and pavilion roofs	wood	$V_2 = 94.2917$	500
Tiles	green tile	$V_3 = 78.0221$	1,800

Table 2. Material information for the superstructure of the model (corridor and pavilion sections).

Where subscripts 1, 2, and 3 represent longitudinal, radial, and tangential directions, respectively; E denotes modulus of elasticity; Nu denotes Poisson's ratio; G denotes shear modulus; f denotes yield stress; and R denotes the ratio of yield stress in each direction. All moduli units in Table 1 are in MPa.

Local material coordinate systems were explicitly defined throughout the complex geometry to accurately capture the orthotropic behavior of timber. For straight members (e.g., beams and columns), the longitudinal axis (1-axis) was aligned with the grain direction, the and radial (2-axis) and tangential (3-axis) orientations were assigned based on the cross-sectional geometry. At the curved sections (arch transitions) and mortise-tenon joints, the coordinate systems were locally reoriented using ABAQUS's orientation tools of ABAQUS to ensure the continuity of the material axes across the connected components, preserving the directional dependencies of the stiffness and strength[31,32].

The substructure abutments for Model 1 and the arch base for Model 2 are modelled as concrete with a density of ρ_c =2400 kg/m³, Young's Modulus of 3×10^{10} Pa, and Poisson's Ratio of 0.2. Its plastic damage behaviour adheres to the Code for design of concrete structures (GB50010-2010), with the stress–strain and damage-strain relationships illustrated in Fig. 6.

The mass of each model component is calculated using its volume, derived from AutoCAD models. The superstructure's material properties (corridors and pavilons) are summarized in Table 2.

The mass calculations for the superstructure components are given by Eq. (2), Eq. (3) and Eq. (4).

The mass of corridor and pavilion frames (m_1):

$$m_1 = 57.2069 \times 500 = 28600 kg \tag{2}$$

The mass of corridor and pavilion roofs (m_2):

$$m_2 = 94.2917 \times 500 = 47100 kg \tag{3}$$

The mass of tiles (m_3):

$$m_3 = 78.0221 \times 1800 = 140000 kg \tag{4}$$

where V_1, V_2, and V_3 represent the volumes of the frames, roofs, and tiles, respectively, as exported from AutoCAD. The substructure's material properties are detailed in Table 3.

The standard values of gravitational loads for both models are calculated as shown in Eq. (5) and Eq. (6).

$$G_{m1} = (m_{11} + m_{12})g = (97200 + 2380000) \times 9.8 = 2.43 \times 10^7 kg \tag{5}$$

$$G_{m2} = (m_{21} + m_{22})g = (49200 + 4090000) \times 9.8 = 4.06 \times 10^7 kg \tag{6}$$

Model	Superstructure component	Materials	Volume (m³)	Density (kg/m³)	Mass (kg)
1	bridge deck	wood	194.4300	500	$m_{11} = 97{,}200$
	piers	concrete	991.3332	2,400	$m_{12} = 2{,}380{,}000$
2	bridge deck	wood	98.4270	500	$m_{21} = 49{,}200$
	bridge body	concrete	1702.7782	2,400	$m_{22} = 4{,}090{,}000$

Table 3. Calculation of the mass of the model substructure.

Model	Loads	Tickers	Type	Characteristic value	Partial safety factor	Combination value
1	Superstructure loads	q_1	Dead load	5.87×10^5 Pa	1.3	7.63×10^5 Pa
	Crowd loads	q_{21}	Live load	3.00×10^3 Pa	1.5	4.50×10^3 Pa
	Self-weight loads	G_{m1}	Gravity	2.43×10^7 N	-	2.43×10^7 N
2	Superstructure loads	q_1	Dead load	5.87×10^5 Pa	1.3	7.63×10^5 Pa
	Crowd loads	q_{22}	Live load	2.9×10^3 Pa	1.5	4.35×10^3 Pa
	Self-weight loads	G_{m2}	Gravity	4.06×10^7 N	-	4.06×10^7 N

Table 4. Load arrangement of the model.

where G_{m1} and G_{m2} are the gravitational loads of Models 1 and 2, respectively; m_{11} and m_{12} are represent the mass of bridge deck and piers of Model 1, respectively; m_{21} and m_{22} are represent the mass of bridge deck and bridge body of Model 2, respectively; $g = 9.8$ m/s² is the gravitational acceleration.

Based on the results in Table 2, the superstructure's distributed load on the bridge deck can be obtained, which is shown in Eq. (7).

$$
\begin{aligned}
q_1 &= \frac{(m_1 + m_2 + m_3)g}{S_p} \\
&= \frac{(2.86 \times 10^4 + 4.71 \times 10^4 + 1.40 \times 10^5) \times 9.8}{3.6} \\
&= 5.87 \times 10^5 Pa
\end{aligned}
\tag{7}
$$

where q_1 is the distributed load on the bridge deck; m_1, m_2 and m_3 denote the mass of corridors and pavilions frames, corridors and pavilion roofs, and tiles, respectively, which shows in Table 1; S_p denotes the contact area between the superstructure of the model (i.e., the corridor and pavilion sections) and the bridge deck, which in this model is 3.6 m²; g denotes the acceleration of gravity, which takes the value of 9.8 m/s².

The crowd load, calculated using the General code for engineering structures (GB55001-2021), is shown in Eq. (8).

$$
Q_{\text{crowd}} = \begin{cases}
3.0, L_0 \leq 50m \\
3.25 - 0.005L_0, 50m < L_0 \leq 150m \ (kN/m^2) \\
2.5, L_0 \geq 150m
\end{cases}
\tag{8}
$$

where Q_{crowd} is the crowd load and L_0 is the maximum calculated span of the bridge.

According to Eq. (3), the crowd load in Model 1 is 3.0 kN/m², and for Model 2, it is 2.9 kN/m².

According to the Unified standard for reliability design of building structures (GB50068-2018), the sub-coefficients γ_G for dead load and γ_Q for live load are 1.3 and 1.5, respectively, and the calculation formulas are shown in Eq. (9).

$$
S = \gamma_G G + \gamma_Q Q
\tag{9}
$$

where S, G and Q denote the load combination values, dead load and live load respectively. The load arrangement of the model is summarisedin Table 4.

The load-acting cross section is shown in Fig. 7, where the red locations indicate the faces of the load arrangement.

rotation that would artificially amplify deck For boundary conditions, the bottom surface of the bridge abutment is coupled to a reference point. In the static analysis, this point is fully fixed. In dynamic analysis, it is unconstrained in the direction of the seismic wave to allow input of the El-Centro seismic excitation. The bridge deck and body are modelled with a tied connection to ensure cohesive behaviour. Regarding soil-structure interaction (SSI), the model explicitly assumes a rigid foundation condition in which soil flexibility is neglected, a simplification justified by the massive stone masonry abutments typical of wind and rain bridges. The reference point coupling method applied at the abutment base enforces complete fixity in the rotational degrees of freedom (R_x, R_y, R_z) during static analysis. For seismic excitation, translational freedom is selectively released only in the seismic wave direction (X-axis), whereas the rotational constraints remain active. This configuration: (a)
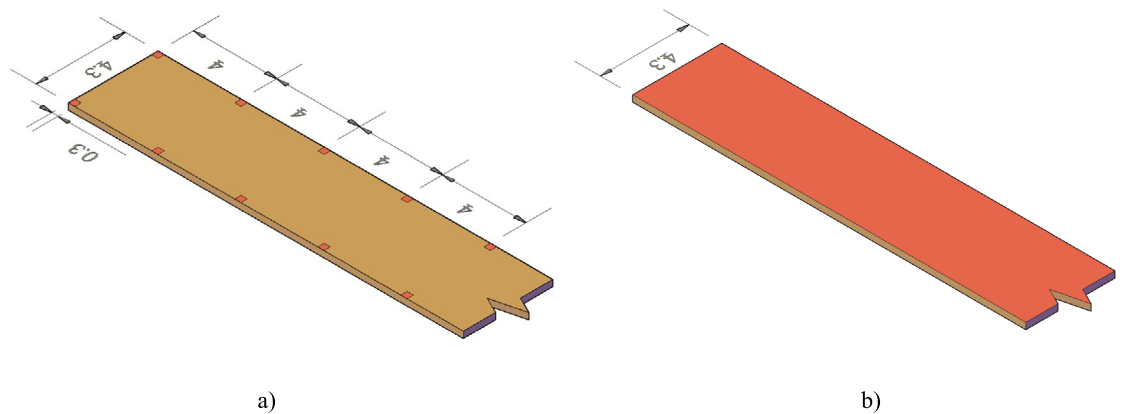
a)　　　　　　　　　　　　　　　　　　　　　　b)

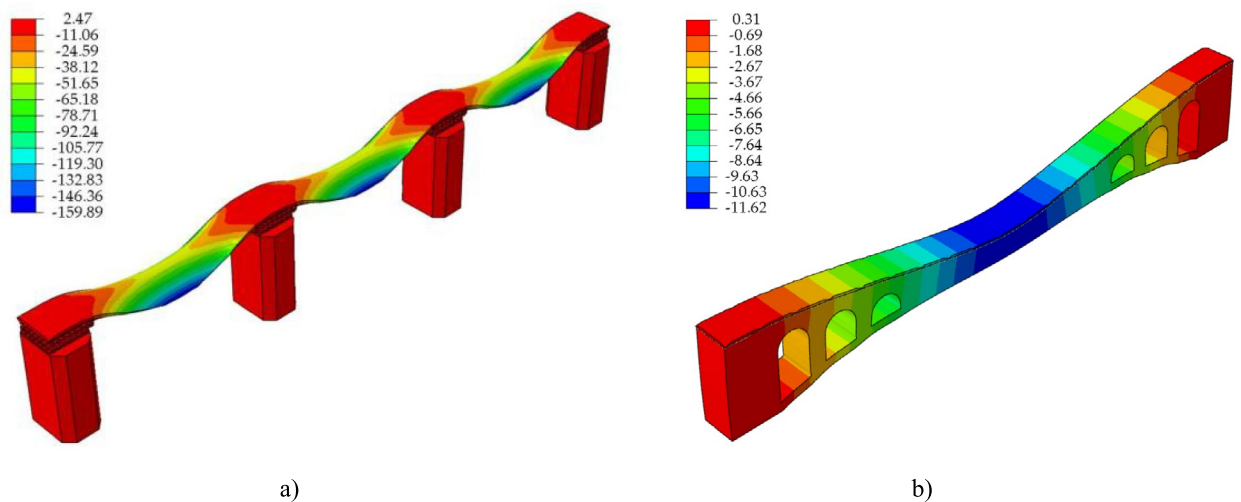**Fig. 7**. Section with loads based on AutoCAD 2020 (URL: https://www.autodesk.com/products/autocad/over view).

a)　　　　　　　　　　　　　　　　　　　　　　b)

Fig. 8. Displacement analysis contours of the model (mm) based on ABAQUS 2024 (URL: https://www.3ds.com/products/simulia/abaqus).

prevents rigid-body displacements, (b) accurately represents the high rotational stiffness of embedded masonry foundations, and (c) allows pure translational input of the El-Centro wave without SSI effects, consistent with the Code for seismic design of buildings (GB50011) recommendations for structures with foundation width/depth ratios > 4.

Model assumptions
The following assumptions are adopted in the finite element modelling of the wind and rain bridge models:

1. Material behaviour is represented using simplified constitutive models (e.g., ideal elastic–plastic, linear-elastic fracture mechanics), ignoring microscopic defects or complex damage mechanisms.

2. Supports and boundary conditions are idealized as fully fixed, hinged, or sliding and disregarding actual connection stiffness or frictional effects.

3. Complex loads are simplified into equivalent nodal or surface forces based on Saint Venant'sprinciple, ignoring local stress concentration effects.

4. Dynamic analysis employs an implicit time integration method, with time steps selected to ensure numerical stability.

Finite element analysis of the model
Static load analysis and comparison of bridge structures
The longitudinal displacements of the bridge structures Model 1 and 2 under the specified loading conditions are shown in Fig. 8.

Finite element analysis reveals maximum mid-span deflections of 159.89 mm for Model 1 and 11.62 mm for Model 2. The deflection of Model 2, representing the arch bridge structure (Xijiang Longtan Bridge), is
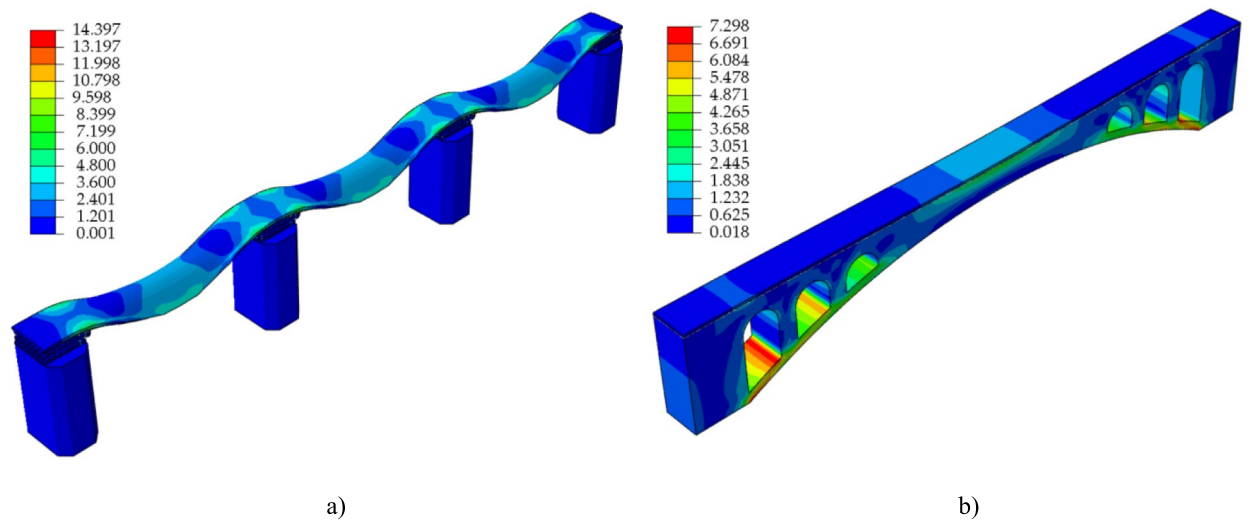
a)   b)

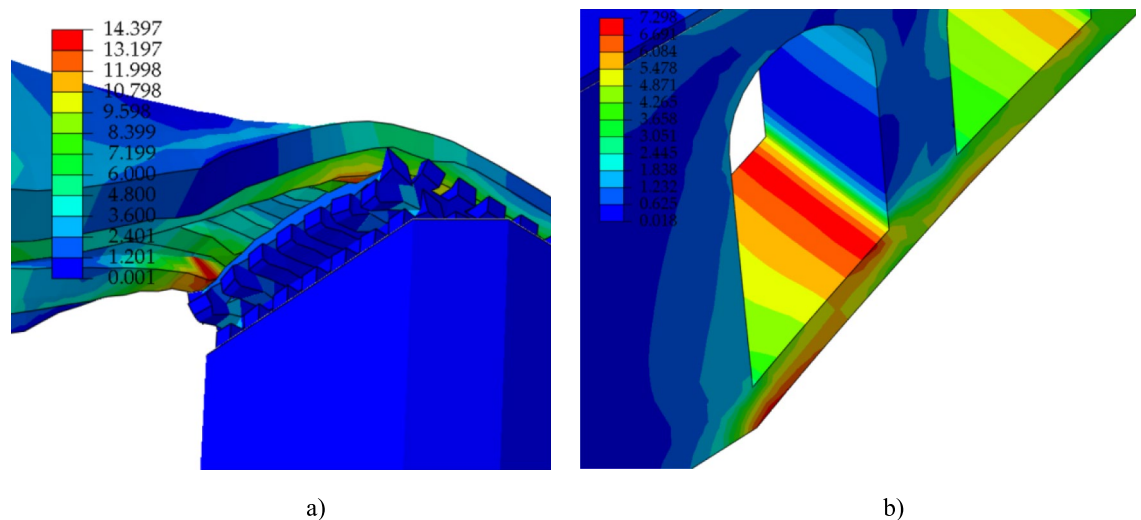**Fig. 9**. Mises stress analysis contours of the model (MPa) based on ABAQUS 2024 (URL: https://www.3ds.com/products/simulia/abaqus).

a)   b)

Fig. 10. The location of the local mises stress maximum of the model (MPa) based on ABAQUS 2024 (URL: https://www.3ds.com/products/simulia/abaqus).

approximately 7.27% of Model 1's, indicating superior load-bearing capacity under identical loads. For Model 1, a three-span simply supported beam bridge structure Chengyang Yongji Bridge), the mid-span deflection is nearly identical across all spans. This uniform deflection distribution reflects consistent stiffness and symmetric load transfer across each span, characteristic of supported bridges where spans bear loads independently with minimal mechanical coupling.

The Mises stress distributions under the same loading conditions are shown in Fig. 9.

In Model 1, the stress distribution is relatively uniform, indicating a balanced stress state. The stress cloud diagram highlights higher equivalent stresses in the upper deck compared to the lower deck, consistent with the bending moment distribution under vertical loads: the upper region experiences tensile stress, while the lower region undergoes compression. Notably, the pier section exhibits near-zero, suggesting minimal stress transfer to the abutments under these conditions.

In contrast, Model 2 exhibits significantly lower overall Mises stress levels, demonstrating improved stress distribution. However, localised stress concentrations are observed, particularly around the perforated sections of the arch, as shown in Fig. 10. These concentrations, likely due to abrupt changes in local stiffness and stress flow redistribution caused by the geometry of the hallow arches, may pose risks to the structures's fatigue life and load-bearing capacity.

According to the stress contours analysis in Fig. 10, the maximum Mises stress of Model 1 occurs at the interface of the bridge deck-pier connection and reaches 14.397 MPa. This stress concentration results from

geometric discontinuity and stiffness mismatch: the rigid deck forms a sharp transition at the pier connection, disrupting the load transfer path. The abrupt change in material stiffness prevents gradual stress attenuation, creating a significant stress gradient. This phenomenon aligns with Saint Venant's principle, where sudden cross-sectional perturb uniform stress field. In contrast, Model 2's maximum equivalent stress, 7.298 Mpa, is observed at two locations: the curvature transition nodes at the arch opening at the arch base. This distribution pattern reflects the arch structure's mechanics, where approximately 70% of the vertical load is transferred via axial compression along the arch ring, following a typical pressure line transfer path. The geometrical continuity of the arch structure ensures a progressive distribution of stresses along the arch axis, with a stress concentration factor of about 49.3% lower than that of Model 1. The peak stress at Model 2's arch base arises from secondary bending moments due to the interaction between foundation reaction forces and arch deformation, a characteristic response of arch structures. Comparison of the two models shows that Model 2 effectively optimises the stress transfer path through the continuity design of the arch structure, and controls the maximum stress level within the allowable strength of the material, which reflects the advantage of the arch structure in dispersing the stress concentration.

To address the identified stress concentrations, we propose an optimization approach. At the level of geometric optimisation, a gradient transition design is adopted for the Model 1 abutment: introducing a curved gradient transition structure instead of a right-angle connection significantly reduces the degree of stress concentration cross-section mutation. Additionally, a gradient composite interlayer with directionally arranged high-strength fibres can be introduced at the connection to smooth stiffness transitions. For the opening of the arch edge of Model 2, a honeycomb hollow topology can be used to disperse the local stress peaks across adjacent units with the help of anisotropic structural characteristics. Regarding structural measures, smart material components can be pre-buried in high-stress areas, triggering active deformation compensation through the monitoring and feedback mechanism to form a dynamic stress-control capability. Construction techniques for Model 1 include surface strengthening at critical nodes and high-frequency vibration to induce a residual compressive layer. As for the monitoring system, a high-density sensor network can be deployed in the stress concentration area, combined with a digital model, to achieve real-time stress field prediction and assessment. For long-term maintenance, non-contact scanning technology is recommended for periodic full-field strain monitoring, with data stored in a lifecycle database to inform maintenance decisions. This multi-dimensional synergistic strategy significantly reduces stress levels and enhances fatigue resistance in critical areas.

(a) Regarding the scales, the strategy systematically operates at the component scale (modifying geometric details, such as abutment transitions and arch openings), material scale (tailoring interfaces with functionally graded materials), and system scale (implementing structural health monitoring networks). (b) Regarding the methodology, parametric geometric optimization was performed to replace sharp corners with smooth curved transitions in the deck-abutment junction of Model 1, topology optimization was performed to introduce controlled honeycomb hollow patterns around the arch openings of Model 2, and material design was performed to create stiffness-graded interlayers via directionally aligned fibers at critical connections. (c) For stress mitigation, these methods directly target stress concentrations: geometric smoothing eliminates stress risers by removing abrupt section changes and redistributing bending moments; topological patterning disperses peak stresses around openings by activating adjacent material paths; and material grading reduces interfacial stress by progressively matching the stiffness between connected components. This integrated approach provides a clear pathway for enhancing the structural durability of critical details.

Vibration modal analysis

The natural frequency and mode shape of the structure were determined by performing nine modal analyses on the two models. Figure 11 shows the response contours of each model in key modes, which visualises the structure's vibration characteristics, providing a critical basis for assessing the dynamic performance and potential resonance risks.

The analysis results show that Model 1's structural response is more significant in the lower-order modes. The vibration amplitudes of the 5th and 6th-order modes are the largest, corresponding to the frequencies of 4.8178 Hz and 4.8234 Hz, respectively. These frequencies primarily exhibit torsional vibrations of the bridge deck. In contrast, the maximum structural response of Model 2 is concentrated in the 2nd and 5th-order modes, whose frequencies are 5.7508 Hz and 10.789 Hz, respectively. The 2nd-order mode reflects the overall transverse vibration of the arch structure, while the 5th-order mode corresponds to the localized vertical vibration of the arch ring.

Rayleigh damping model is applied to characterised the system's damping behaviour, expressed as:

$$[C] = \alpha[M] + \beta[K] \tag{10}$$

where C, M and K denote the damping, mass and stiffness of the model respectively.

Its solution is given by

$$\alpha = \frac{4\pi f_i f_j \xi}{f_i + f_j} \tag{11}$$

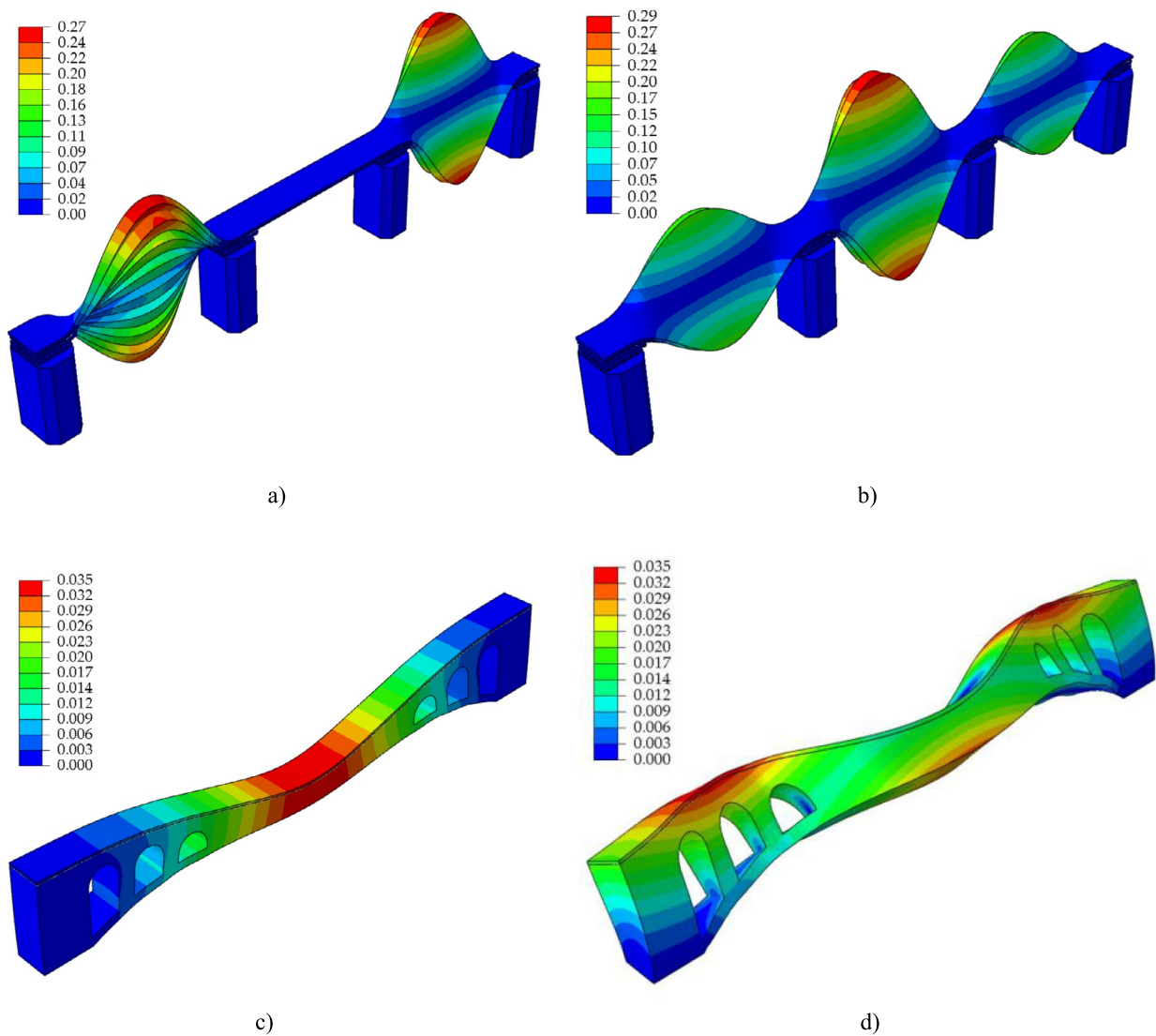$$\beta = \frac{\xi}{\pi(f_i + f_j)} \tag{12}$$

Fig. 11. Structural response contours for the two modes with the largest structural response in the modal analysis (mm) based on ABAQUS 2024 (URL: https://www.3ds.com/products/simulia/abaqus).

Model	Materials	ξ	f_i (Hz)	f_j (Hz)	α	β
1	concrete	0.05	4.8178	4.8234	1.51444	0.00099
	wood	0.03			0.90866	0.00165
2	concrete	0.05	5.7508	10.789	2.35700	0.00096
	wood	0.03			1.41420	0.00058

Table 5. Calculation of α-β damping factor.

where ξ denotes the material damping ratio, set to 0.05 for concrete and 0.03 for wood. f_i, f_j denote the frequencies corresponding to the two largest modes of the structural response in the modal analysis, respectively. The α-β damping coefficients are calculated as shown in Table 5.

Seismic Wave Loading and Analysis Setup.

The El-Centro earthquake wave, recorded during the Masy 18, 1940, Imperial Valley earthquake, is selected as the excitation input for both models, with its acceleration time-history curve in Fig. 12.

To ensure the engineering convenience of the study, El-Centro seismic waves were selected as the dynamic input for the finite element analysis in this study. It was chosen primarily because of its broad characterization, moderately strong spectral content, and well-documented acceleration time history, which effectively covers the key phases of structural excitation (initial impulse loading, sustained strong motion, and decay). These
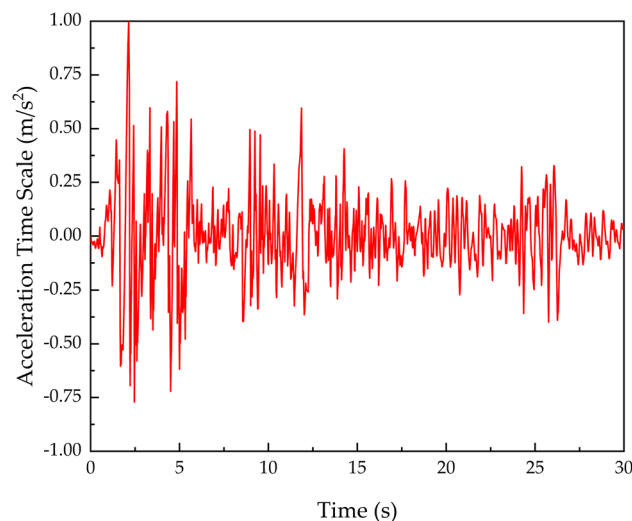
Fig. 12. Time scale analysis of El-Centro earthquake wave based on Origin 2021 (URL: https://www.originlab .com/).

characteristics robustly excite multi-order vibration modes and engage key nonlinear phenomena, such as ductility demands, energy dissipation pathways, and inherent damping mechanisms, which are highly relevant to the seismic vulnerability assessment of complex traditional timber structures, such as wind-and-rain bridges. To align directly with specific national design code provisions, the record was scaled to a Peak Ground Acceleration (PGA) of 0.35 m/s^2. This PGA level corresponds explicitly to the Code for seismic design of buildings (GB50011-2001) requirement for ground motion intensity under frequent earthquakes (seismic fortification intensity of seven degrees) for this structure category and site conditions. Furthermore, utilizing the full 30-s strong motion segment, followed by the specified 5-s interval for assessing residual vibrations, allows for a comprehensive evaluation of the structural response from the initial yield to post-peak behavior and free-vibration decay.

While recognizing that modern seismic assessment standards and best practices increasingly emphasize analyzing multiple ground motions to account for record-to-record variability and enhance statistical robustness, the focused use of El-Centro in this initial phase serves a specific comparative and diagnostic purpose. Its status as a universal standard provides a critical baseline against which future numerical models and experimental findings can be reliably calibrated and compared, ensuring internal consistency in the foundational study. This facilitates the validation of the complex finite element model against a well-understood seismic input before extending the analysis.

Comparison of seismic performance

The acceleration time-history contours at various time points, shown in Fig. 13, illustrate the dynamic response of Models 1 and 2 under seismic excitation.

As shown in Fig. 14, mid-span positions (points A and B) were selected to evaluate acceleration and displacement responses under the El-Centro seismic wave, highlighting non-uniform dynamic characteristics.

The results are presented in Fig. 15 and Fig. 16.

The acceleration time-history analysis in Fig. 15 reveals that Model 1's peak acceleration response in the seismic wave direction significantly exceeds that of Model 2. At point B, Model 2's peak acceleration is 68.31% of Model 1's, and at point A, it is only 49.08%. This result indicates that the arch bridge structure, represented by the Xijiang Longtan Bridge, exhibits better seismic performance due to its mechanical force transfer path, leveraging axial compression to dissapate energy. In contrast, the simply supported beam bridge structure, represented by Chengyang Yongji Bridge, has a significant acceleration response and a relatively weaker seismic performance due to the lack of a horizontal thrust mechanism.

According to the displacement time course curves in Fig. 16, the displacement responses of the two models in the direction of seismic waves are closely aligned, with a maximum difference of less than 5%. This similarity suggests comparable global stiffness under identical seismic input. However, despite the similar displacement response, Model 2's acceleration response is significantly lower than that of Model 1, indicating that the arch bridge structure has obvious advantages in energy dissipation and vibration control. This finding underscore the arch bridge's suitability for seismic-prone regions and provide valuable insights for bridge seismic design.

Model 1 mainly exhibits the failure of connection node degradation and poor structural integrity characteristics under strong seismic effects. During the seismic action, the maximum stress at the deck-pier connection node reaches 13.2449 MPa, higher than under static loading, as shown in Fig. 17. Mortise-and-tenon joints between spans accumulate slip deformation under cyclic seismic loads, exacerbated by wood's anisotropic properties, leading to node stress relaxation. The bridge deck's composite transverse bending and longitudinal torsion create a weak mid-span interface under biaxial tension. Seismic energy input causes initial cracking at the deck-abutment geometric transition, triggering local stiffness degradation. Non-cooperative deformation across spans amplifies displacement differences, risking inter-span collisions and progressive collapse.
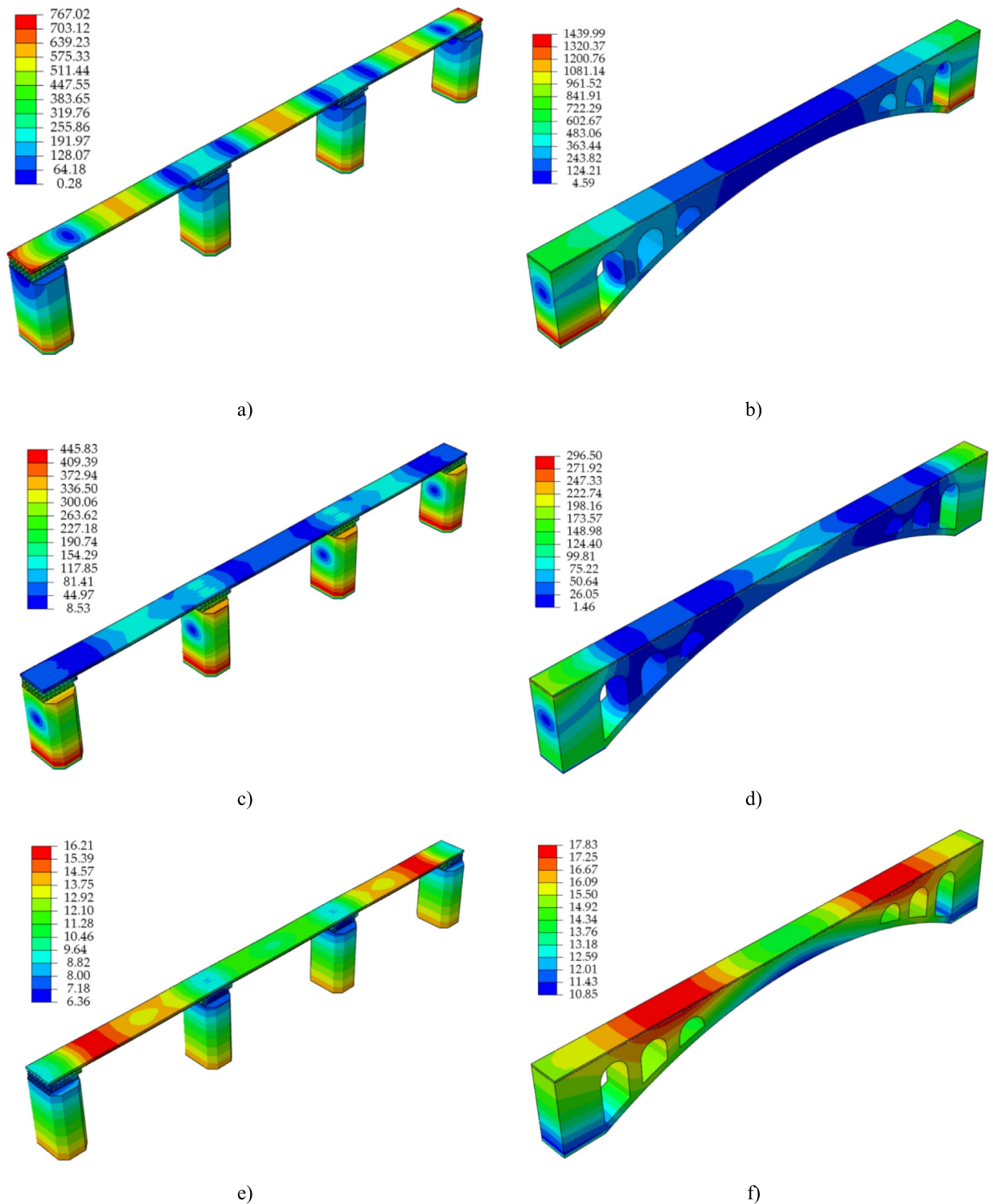
Fig. 13. Acceleration time-history contours for Models 1 and 2 at selected time points (mm/s²) based on ABAQUS 2024 (URL: https://www.3ds.com/products/simulia/abaqus).

In Model 2, failure risks concentrate at the arch base, where the maximum stress reaches 8.60593 MPa during seismic loading, as shown in Fig. 18. Under combined axial compression and transverse seismic forces, the concrete arch base develops oblique shear cracks with accumulating plastic damage. Curvature discontinuities at the arch base redistribute stress flow, forming a principal stress node that accelerates the spalling of the concrete protective layer and the collapse of the core zone. Although local vibrations in auxiliary arches may induce higher-order responses, seismic energy primarily transfers through the arch ribs to the base. The small displacement variations at the base constraints disrupt the axial pressure balance of the arch, triggering the
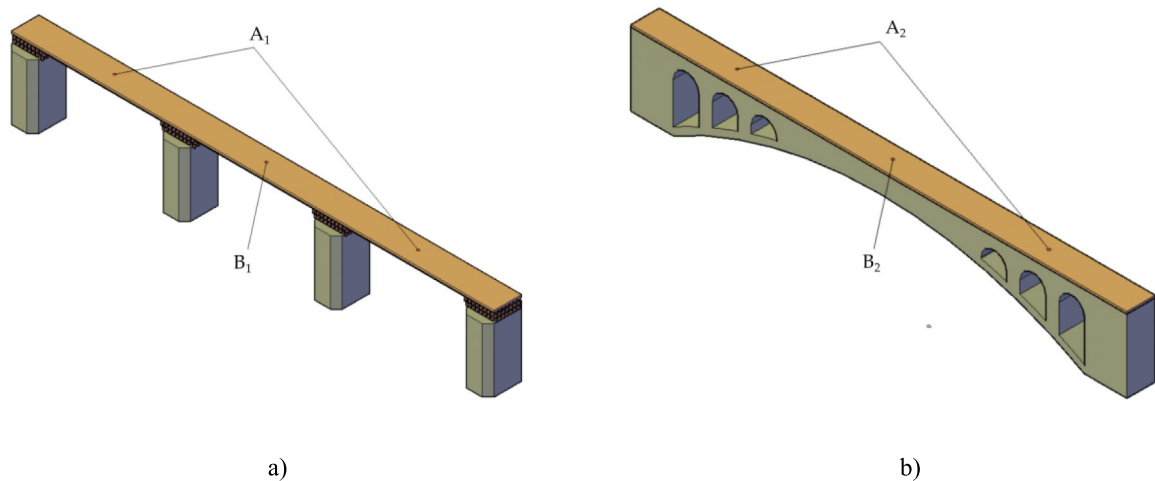
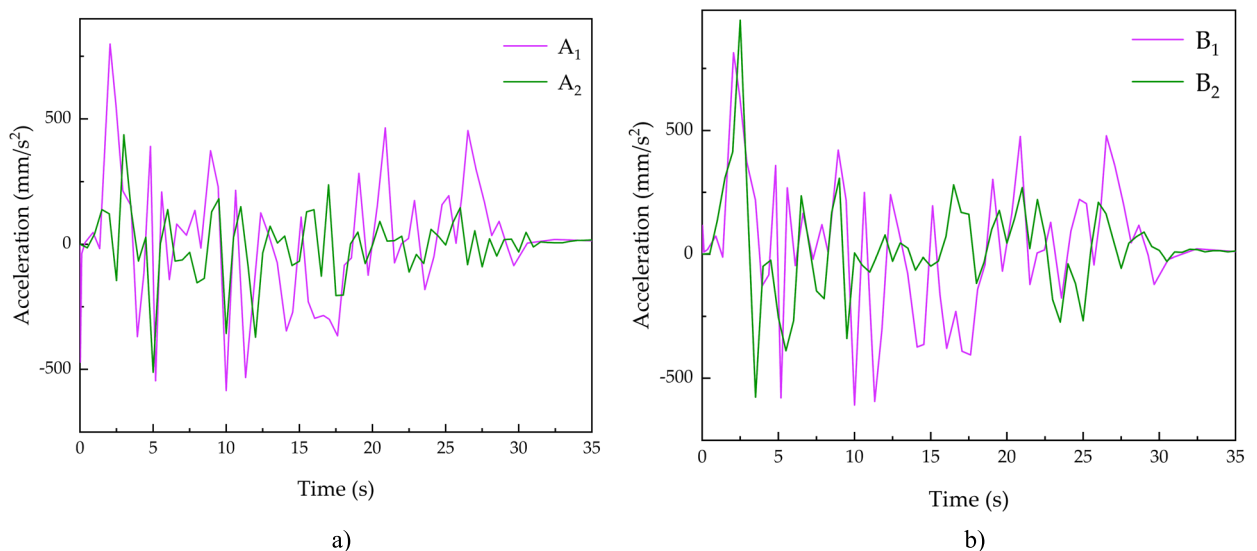Fig. 14. Analysing point selection based on AutoCAD 2020 (URL: https://www.autodesk.com/products/autocad/overview).

Fig. 15. Time-history of mid-span acceleration at points **A** and **B** under El-Centro seismic wave based on Origin 2021 (URL: https://www.originlab.com/) and ABAQUS 2024 (URL: https://www.3ds.com/products/simulia/abaqus).

instability of the thrust system. The overall failure manifests as a chain reaction following arch base damage, with a risk of sudden overturning.

Conclusions

This study investigates the structural and seismic performance of wind and rain bridges, traditional Dong ethnic minority architecture, to provide a scientific foundation for their preservation and cultural inheritance. Through detailed finite element analysis of the simply supported beam bridge (Model 1), represented by Chengyang Yongji Bridge, and the arch bridge structure (Model 2), represented by Xijiang Longtan Bridge, significant differences in load-bearing capacity, deformation characteristics, and seismic response are revealed. The numerical simulations, conducted using ABAQUS, systematically evaluate the mechanical and seismic properties of these wooden structures, offering technical insights for their optimization and contributing to the sustainable development of cultural heritage. The main conclusions are as follows:

The arch bridge (Model 2) significantly outperforms the simply supported beam bridge (Model 1) in load-bearing capacity. Mid-span deflections are 159.89 mm for Model 1 and 11.62 mm for Model 2, the latter being approximately 7.27% of the former. Model 1's Mises stress distribution is uniform, with higher tensile
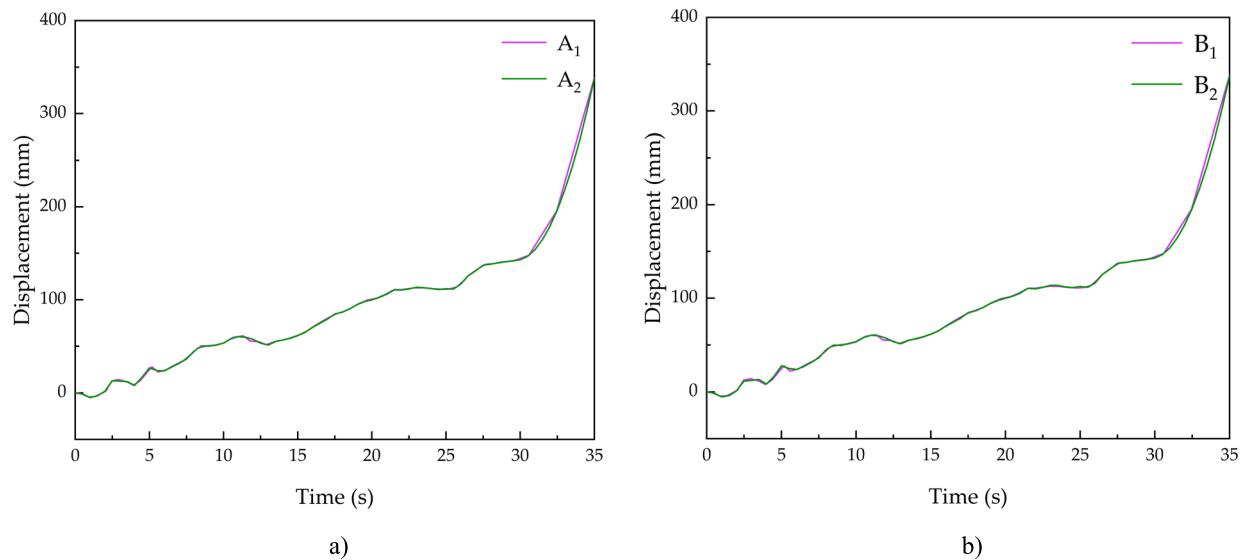
Fig. 16. Time-history of mid-span displacement at points **A** and **B** under El-Centro seismic wave based on Origin 2021 (URL: https://www.originlab.com/) and ABAQUS 2024 (URL: https://www.3ds.com/products/simulia/abaqus).
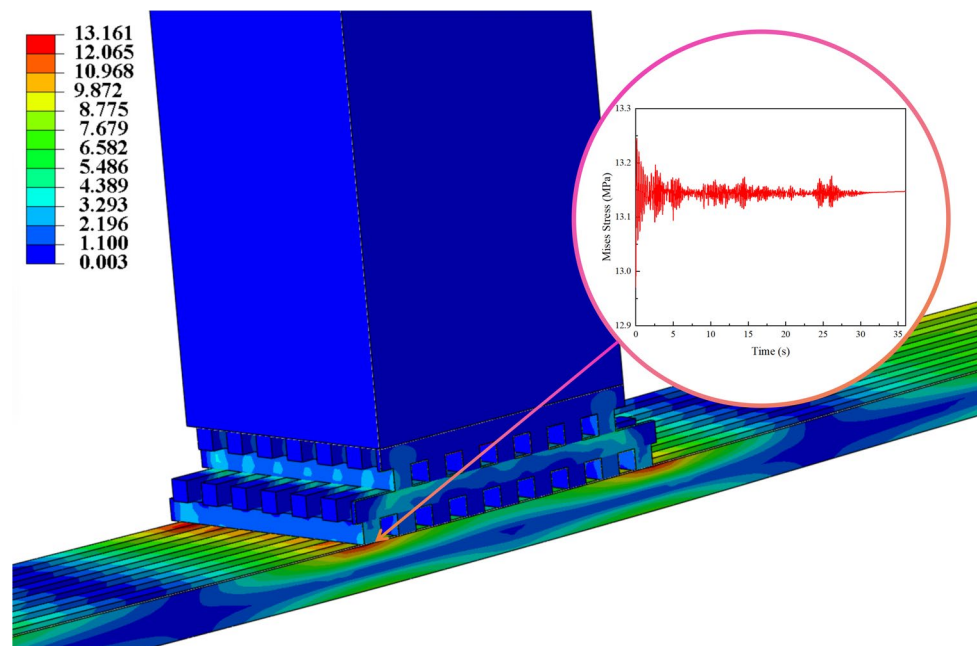

Fig. 17. Maximum stress locations and stress variations in Model 1 during seismic loading based on Origin 2021 (URL: https://www.originlab.com/) and ABAQUS 2024 (URL: https://www.3ds.com/products/simulia/abaqus).

stresses in the upper deck than compressive stresses in the lower deck and near-zero stress at piers, indicating minimal stress transfer to abutments. In contrast, Model 2's overall equivalent stress level is significantly lower than that of Model 1, but it forms a significant stress concentration area around the hallow arch openings. The maximum stresses of Model 1 are 14.397 MPa at the junction of the bridge deck-abutment interface and 7.298 MPa at Model 2's arch opening edges and base, highlighting the arch's superior stress distribution.

Nine-mode modal analysis reveals distinct vibration characteristics. Model 1's largest responses occur in the 5th and 6th modes at 4.8178 Hz and 4.8234 Hz, characterized by transverse bending and longitudinal torsional deck vibrations. Model 2's peak responses occur in the 2nd mode at 5.7508 Hz, reflecting overall transverse arch vibration, and the 5th mode at 10.789 Hz, reflecting localized vertical arch ring vibration, indicating higher modal stiffness than Model 1.
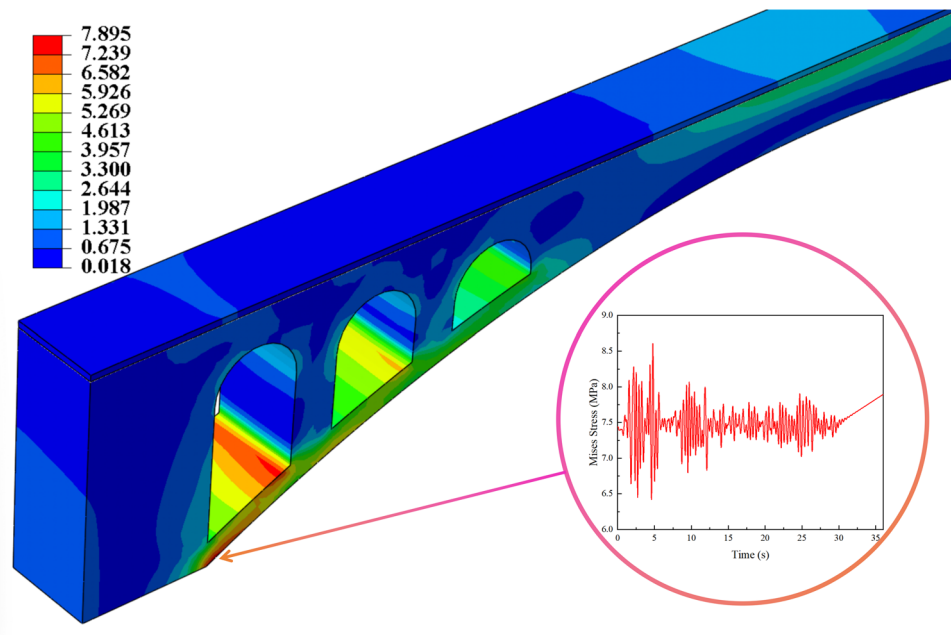
Fig. 18. Maximum stress locations and stress variations in Model 2 during seismic loading based on Origin 2021 (URL: https://www.originlab.com/) and ABAQUS 2024 (URL: https://www.3ds.com/products/simulia/abaqus).

Time-history analysis using El-Centro seismic waves, based on a 7-degree fortification standard, demonstrates Model 2's superior seismic performance. Peak acceleration responses at mid-span points A and B were 49.08% and 68.31% of Model 1's, respectively, due to Model 2's (arch bridge structrure) efficient energy dissipation via axial compression. Model 1's higher accelerations reflect weaker seismic resistance due to the lack of a thrust mechanism.

The arch bridge demonstrates superior load-bearing and seismic performance, with stress concentration points at the deck-abutment interface for Model 1 and the arch base for Model 2, offering technical insights for restoration and reinforcement. Wind and rain bridges, a hallmark of the Dong ethnic minority's traditional architecture and other ethnic minorities, integrating bridges, pavilions, and corridors, showcase unique construction techniques and cultural value. This study's scientific analysis supports their preservation, promotes ethnic and cultural diversity, and informs sustainable regional development.

Further finite element model validation is recommended using 1:10 scaled physical models with anisotropic timber matching the prototypes. Static load tests with strain gauges at key nodes (e.g., mid-span, arch shoulder) measure strain distributions, which are converted to stresses to verify that the stress concentration in the arch bridge is lower than that in the simply supported beam bridge, using loads scaled per similarity laws for a 1:10 model to ensure stress equivalence. Modal tests using the hammering method with accelerometers measure the first six modes' frequencies and shapes, confirming Model 2's higher natural frequencies, indicating greater modal stiffness. Seismic simulation is conducted by inputting scaled El-Centro waves into the shaker, monitoring strain and displacement responses using a fibre optic grating sensor and analyzing the spectral attenuation characteristics of the acceleration response to verify Model 2's reduced acceleration response. Cross-validation of experimental and simulated stresses, frequencies, and acceleration responses within a 5% error margin quantitatively assesses the model's accuracy.

This study compares the advantages and disadvantages of two different structural models of wind and rain bridges in terms of static load-carrying capacity and dynamic seismic capacity. However, this study still has some limitations in the universality of the selection of seismic waves and the design of the damping scheme, which need to be addressed in subsequent studies. Future research should explore vibration-damping techniques specifically targeting the critical failure modes identified in this study. For Model 1 (simply supported), where the seismic analysis revealed significant stress concentration and potential joint degradation at the deck-pier connections under cyclic loading (peak stress 13.2449 MPa), integrating viscous dampers compatible with mortise-and-tenon joints directly at these interfaces could enhance energy dissipation and mitigate slip deformation, thereby preserving structural integrity without altering aesthetics. Conversely, for Model 2 (arch bridge), where the seismic failure risk is concentrated at the arch base (peak stress 8.60593 MPa), the installation of lightweight friction dampers at this location could effectively reduce the shear stresses. Furthermore, exploring Seesaw systems with fluid viscous dampers, potentially incorporating soil-structure interaction if foundation conditions permit, could address the arch base instability risk identified under seismic excitation[35]. Smart materials pre-buried in high-stress zones, as suggested in our optimization approach, paired with real-time strain sensors, offer adaptive damping potential for both models. Crucially, all strategies

must prioritize non-invasive designs to safeguard the invaluable cultural heritage of bridges, ensuring their resilient and sustainable preservation in seismic regions.

Data availability

All data generated or analyzed during this study are included in this article, the data used in this paper are original data. And the datasets used and/or analyzed during the current study available from the corresponding author on reasonable request.

References

1. Luo, F., Isa, M. I. & Roosli, R. Research status and development direction of smart heritage: a bibliometric review (1994–2024). Journal of Asian Architecture and Building Engineering, 1–24, https://doi.org/10.1080/13467581.2024.2397104 (2024).
2. Yang, C. X., Hu, Y. Q., Su, Q. M., Li, X. J. & Zhu, M. L. Empirical methods for recognizing and evaluating cultural heritage value of Timber-Arched Lounge Bridge from the perspective of cultural memory. *J. Asian Architecture Build. Eng.* https://doi.org/10.1080/13467581.2024.2399689 (2024).
3. Wu, P. J., Li, X. W., Feng, Y. F. & Liu, Y. The impact and transformation evaluation of art intervention in public space on ancient villages: a case study of Tengchong. *Yunnan Province. Sci. Rep.* **15**, 2354. https://doi.org/10.1038/s41598-025-87008-5 (2025).
4. Liu, Y. Application of Digital Technology in Intangible Cultural Heritage Protection. *Mob. Inf. Syst.* **2022**, 7471121. https://doi.org/10.1155/2022/7471121 (2022).
5. Dong, Q. L., Wei, T. H., Wang, Y. & Zhang, Q. P. Intangible cultural heritage based on finite element analysis: force analysis of Chinese traditional garden rockery construction. *Heritage Sci.* **12**, 241. https://doi.org/10.1186/s40494-024-01355-6 (2024).
6. Xie, L., He, X. H., Hu, Y. X., Wei, X. J. & Shen, L. Wooden Cantilever Covered Bridges in Anhua, China. Bioresources, 18, 4182–4194, https://doi.org/10.15376/biores.18.2.4182-4194 (2023).
7. Hong, Y. Architectural Characteristics of Enshi Wind-Rain Bridge. *Front. Green Build, Mater. Civil Eng. III, PTS* **1–3**(368–370), 1450–1453. https://doi.org/10.4028/www.scientific.net/AMM.368-370.1450 (2013).
8. Luo, L., Wu, Y. Q. , He, X. & Qin, W. K. Analysis of Building Materials for Wind and Rain Bridge. Materials Science, Energy Technology and Power Engineering III (MEP 2019), 2154, 1450–1453, https://doi.org/10.1063/1.5125378 (2019).
9. Aira, J. R., Cabo-Fernández, M. C., del Blanco-García, F. L. & Gonzalo-Calderón, L. Timber bridges with reciprocal structure. Comparative analysis of the traditional Chinese bridge and the Leonardo bridge. Informes de la Construcción, 74, 565, https://doi.org/10.3989/IC.85874 (2022).
10. Chen, S. J., Yang, Y. & Shen, Z. J. Impact of new construction activities of min-zhe wooden arch bridge in the conservation of its traditional building craftsmanship. *Int. J. Architectural Heritage* **17**, 1207–1220. https://doi.org/10.1080/15583058.2021.2023694 (2023).
11. Brühl, F., Kuhlmann, U. & Jorissen, A. Consideration of plasticity within the design of timber structures due to connection ductility. *Eng. Struct.* **33**, 3007–3017. https://doi.org/10.1016/j.engstruct.2011.08.013 (2011).
12. Liu, R., Hou, M. Y., Liu, X. & Wang, R. H. Analysis on seismic damage of timberwork building and reinforcement. *Construction and Urban Planning, PTS* **1–4**(671–674), 1390–1393. https://doi.org/10.1080/15583058.2021.2023694 (2013).
13. Miebach, F. Design ideas for solid timber bridges. *Wood Mat. Sci. Eng.* **13**, 184–189. https://doi.org/10.1080/17480272.2018.1463291 (2018).
14. Kim, K. H. E. & Andrawes, B. Multihazard Assessment and Retrofit of Deteriorated Timber Pile Bridges. *J. Perform. Constr. Facil.* **32**, 04018020. https://doi.org/10.1061/(ASCE)CF.1943-5509.0001157 (2018).
15. Carrillo, M.; Carreón, H. & Raya, D. Determination of the acoustic anisotropy on a recent and aged Mexican pine wood by ultrasound. Nondestructive Characterization and Monitoring of Advanced Materials, Aerospace, Civil Infrastructure, and Transportation VIX, 11380, https://doi.org/10.1117/12.2557085 (2020).
16. Brémaud, I., Gril, J & Thibaut, B. Anisotropy of wood vibrational properties: dependence on grain angle and review of literature data. *Wood Sci. Technol.* **45**, 735–754 (2011).
17. Phan, N. T., Auslender, F., Gril, J & Pitti, R. M. Effects of cellulose fibril cross-linking on the mechanical behavior of wood at different scales. *Wood Sci. Technol.* **58**, 1555–1583. https://doi.org/10.1007/s00226-024-01569-8 (2024).
18. Faggiano, B., Marzo, A., Formisano, A. & Mazzolani, F. M. Innovative steel connections for the retrofit of timber floors in ancient buildings: A numerical investigation. *J. Rock Mechan. Geotech. Eng.* **87**, 1–13. https://doi.org/10.1016/j.compstruc.2008.07.005 (2009).
19. Yuan, W. H. et al. A dynamic large-deformation particle finite element method for geotechnical applications based on Abaqus. *Wood Mat. Sci. Eng.* **15**, 1859–1871. https://doi.org/10.1016/j.jrmge.2022.09.014 (2023).
20. Dong, Y. F., Zhang, W. Y., Shamsabadi, A., Shi, L. & Taciroglu, E. A vehicle-bridge interaction element: Implementation in ABAQUS and verification. *Appl. Sci.-Basel* **13**, 8812. https://doi.org/10.3390/app13158812 (2023).
21. Ahmad, A. et al. Non-linear finite element modeling of damages in bridge piers subjected to lateral monotonic loading. *Sci. Rep.* **13**, 13461. https://doi.org/10.1038/s41598-023-39577-6 (2023).
22. Kouroussis, G., Ben Fekih, L. & Descamps, T. Using experimental modal analysis to assess the behaviour of timber elements. *Mechan. Industry* **18**, 804. https://doi.org/10.1051/meca/2017042 (2017).
23. Ostrycharczyk, A. W. & Malo, K. A. Network arch timber bridges with light timber decks and spoked configuration of hangers-Parametric study. *Eng. Struct.* **253**, 113782. https://doi.org/10.1016/j.engstruct.2021.113782 (2022).
24. Schönherr, J. A., Schneider, P. & Mittelstedt, C. Robust hybrid/mixed finite elements for rubber-like materials under severe compression. *Comput. Mechanic* **70**, 101–122. https://doi.org/10.1007/s00466-022-02157-y (2022).
25. Iraola, B., Cabrero, J. M., Basterrechea-Arévalo, M. & Gracia, J. A geometrically defined stiffness contact for finite element models of wood joints. *Eng. Struct.* **235**, 112062. https://doi.org/10.1016/j.engstruct.2021.112062 (2021).
26. Nascimbene, R., Fagà, E. & Moratti, M. Seismic strengthening of elevated reinforced concrete tanks: Analytical framework and validation techniques. *Buildings* **14**, 2254. https://doi.org/10.3390/buildings14072254 (2024).
27. Nascimbene, R. Numerical model of a reinforced concrete building: Earthquake analysis and experimental validation. *Periodica Polytechnica-Civil Engineering* **59**, 521–530. https://doi.org/10.3311/PPci.8247 (2015).
28. Ercan, E. Assessing the impact of retrofitting on structural safety in historical buildings via ambient vibration tests. *Constr. Build. Mater.* **164**, 337–349. https://doi.org/10.1016/j.conbuildmat.2017.12.154 (2018).
29. Yang, D. L. & Liu, Y. L. Finite-element analysis of vertical displacement of laminated rubber bearing under earthquake action for disaster resilience of the smart city. *J. Adv. Transp.* **2022**, 7574272. https://doi.org/10.1155/2022/7574272 (2022).
30. Nascimbene, R., Brunesi, E. & Sisti, A. Expeditious numerical capacity assessment in precast structures via inelastic performance-based spectra. *Heliyon* **10**, e39729. https://doi.org/10.1016/j.heliyon.2024.e39729 (2024).
31. Nascimbene, R. An arbitrary cross section, locking free shear-flexible curved beam finite element. *Int. J. Comput. Methods Eng. Sci. Mech.* **14**, 90–103. https://doi.org/10.1080/15502287.2012.698706 (2013).

32. Nascimbene, R. Penalty partial reduced selective integration: a new method to solve locking phenomena in thin shell steel and concrete structures. *Curved Layered Struct.* **9**, 352–364. https://doi.org/10.1515/cls-2022-0027 (2022).
33. Katsimpini, P., Papagiannopoulos, G. & Hatzigeorgiou, G. A thorough examination of innovative supplementary dampers aimed at enhancing the seismic behavior of structural systems. *Appl. Sci.-Basel* **15**, 1226. https://doi.org/10.3390/app15031226 (2025).
34. Cho, C. B., Kim, Y. J., Chin, W. J & Lee, J. Y. Comparing rubber bearings and eradi-quake system for seismic isolation of bridges. *Materials* **13**, 5247. https://doi.org/10.3390/ma13225247 (2020).
35. Katsimpini, P., Papagiannopoulos, G. & Hatzigeorgiou, G. Seismic response of a cable-stayed bridge with concrete-filled steel tube (CFST) pylons equipped with the seesaw system. *GeoHazards* **5**, 1074–1092. https://doi.org/10.3390/geohazards5040051 (2024).
36. Katsimpini, P. S., Papagiannopoulos, G. & Hatzigeorgiou, G. Nonlinear analysis of bridges considering soil-structure interaction and travelling wave effects under combined train and near-fault seismic loads. *Appl. Sci.-Basel* **14**, 11688. https://doi.org/10.3390/app142411688 (2024).
37. Kontoni, D. P. N. & Farghaly, A. A. The effect of base isolation and tuned mass dampers on the seismic response of RC high-rise buildings considering soil-structure interaction. *Earthquakes Struct.* **17**, 425–434. https://doi.org/10.12989/eas.2019.17.4.425 (2019).
38. Yuan, W. K. et al. Seismic performance analysis of wind and rain bridge structures and design of a seismic vibration damping program using rubber isolators. *Structures* **79**, 109474. https://doi.org/10.1016/j.istruc.2025.109474 (2025).

Author contributions

W.Y. constructed the model and carried out finite element analysis, W.Y. wrote and translated the article into English, X.H. and J.L. searched the literature and conducted research work, T.D. provided guidance. All authors reviewed the manuscript.

Funding

Declarations

Competing interests

The authors declare no competing interests.

Additional information

Correspondence and requests for materials should be addressed to T.D.

Reprints and permissions information is available at www.nature.com/reprints.

Publisher's note Springer Nature remains neutral with regard to jurisdictional claims in published maps and institutional affiliations.